

SUPPLEMENTARY INFORMATION

a



b

XPB1 (443 nt)

GGGAGACCCAAGCUGGCUAGCGUUUAAACUUAAGCUCGCCCUCACCAUGGACUACAAAGACGAUGAC
GACAAGCUUGUGGUGGCAGCGGCGCCGAGCGCGGCCACGGCGGCCCCCAAAGUGCUACUCUUAUCU
GGCCAGCCCGCCUCCGUCGGCCGGGCGCUGCCGCUCAUGAUACCCGGUCCGCGGGAAGCAGGGUC
GGAGGCGAGCGGGACACCGCAGGCUCGCAAGCGGCAGCGCUUGGGAUUGGACACGCUGGAUCCUG
ACGAGGUUCCAGAGGUGGAGGCCAAGGGGAGUGGAGUAAGGCUGGUGGCCGGGUCUGCUGAGUCC
GCAGCACUCAGACUACGUGCACCUCUGCAGCAGGUGCAGGCCAGUUGUCACCUCUCCCAAGAACUUCU
UCCCGUGAGCAAGGGCGAGGAGCUGUUCACCGGGGUGGUGCCCAUCC

XPB1/Pst (354 nt)

GGGAGACCCAAGCUGGCUAGCGUUUAAACUUAAGCUCGCCCUCACCAUGGACUACAAAGACGAUGAC
GACAAGCUUGUGGUGGCAGCGGCGCCGAGCGCGGCCACGGCGGCCCCCAAAGUGCUACUCUUAUCU
GGCCAGCCCGCCUCCGUCGGCCGGGCGCUGCCGCUCAUGAUACCCGGUCCGCGGGAAGCAGGGUC
GGAGGCGAGCGGGACACCGCAGGCUCGCAAGCGGCAGCGCUUGGGAUUGGACACGCUGGAUCCUG
ACGAGGUUCCAGAGGUGGAGGCCAAGGGGAGUGGAGUAAGGCUGGUGGCCGGGUCUGCUGAGUCC
GCAGCACUCAGACUACGUGCACCUC

HAC1 (514 nt)

ACUUCAUGGGAGCUGCAGAUGUUUAAAGACGGAAAAUGUACCAGAGUCGACGACGCUACCUGCCGUA
GACAACAACAAUUUGUUUGAUGCGGUGGCCUCGCCGUUGGCAGACCCACUCUGCGACGAUUAAGCG
GAAACAGUCUACCCUUUGACAAUUAUUGAUCUUGACAAUUGGCGUAAUCCAGCCGUGAUUACGA
UGACCAGGAAACUACAGUGAACAAGAACACUAGCCCCAGCUUUUGCUUUCUGCUUUUUUUCUUUUUU
UUUUUUUUUAGUCGUGGUUCUCUGAUGGGGGAGGAGCCGGUUAAAGUACCUUCAAAGCAGAAUGC
AGGGUUUUUUGGAAGCUUUUUUUUUUUUUUUGCUAGUUUUUCCUGAACAAUAGAGCCAUCUUU
UCUUUUUACUAAAGAAUGGACGGCUUGCUUGUACUGUCCGAAGCGCAGUCAGGUUUUGAAUUAUUUG
AAUUGAAUGAUUUUCUUAUCACUUAUGAAGACAAUCGCAAGAGGGUA

HP21

UGCACCUCUGCAGCAGGUGCA

HAC1 28-mer

GCUUGUACUGUCCGAAGCGCAGUCAGGU

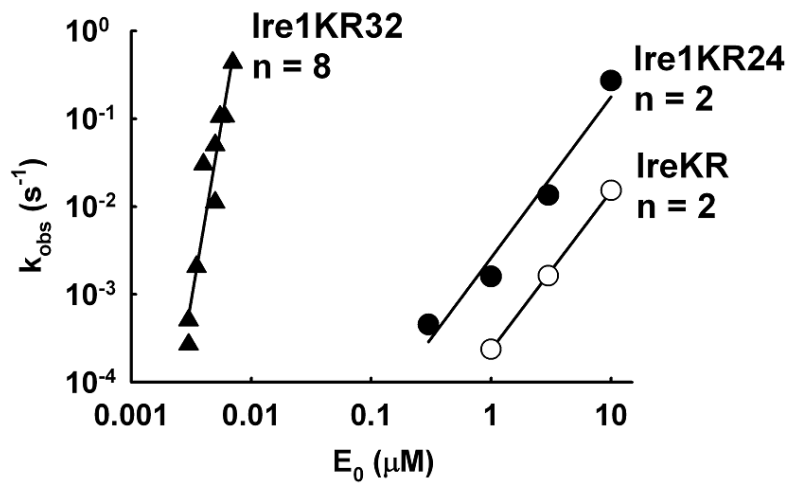
XPB1 58-mer

GGGUCUGCUGAGUCCGACGACUCAGACUACGUGCACCUCUGCAGCAGGUGCAGGCC

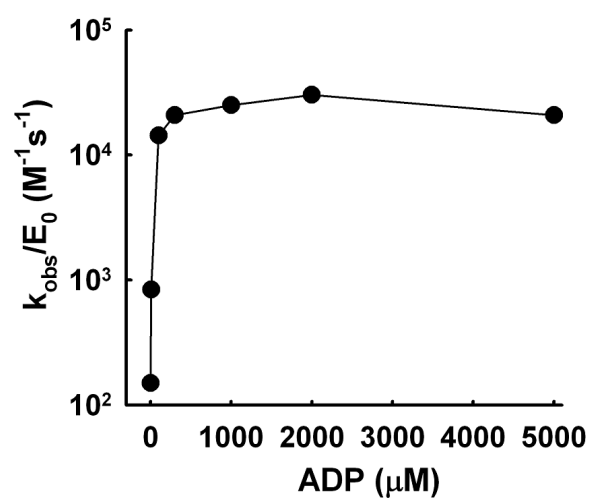
Supplementary Figure 1 | Sequences of protein and RNA constructs used. a,

Constructs used for crystallization of the Ire1 dimer (2rio_full, Lee et al., Cell, 2008) and

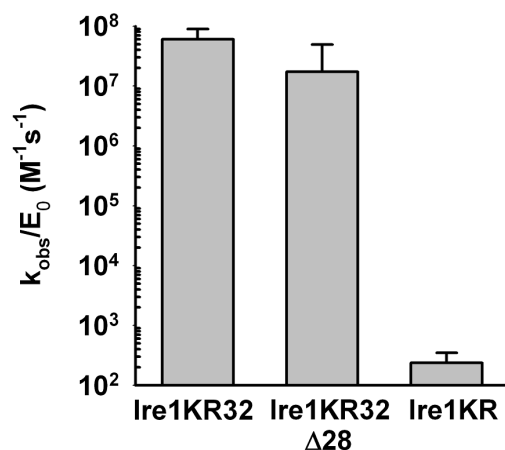
of the Ire1 oligomer with the α F- α EF loop deleted (Ire1KR32 Δ 28) are aligned with the corresponding sequences observed in the crystal structures. **b**, RNA substrates used in this study. Intron sequences are highlighted in dark red. *XPB1*/PstI was obtained via restriction cleavage of *XPB1* 443-mer encoding plasmid with PstI endonuclease. The PstI cleavage site is located in *XPB1* mRNA prior to the second splice site and eliminates the second stem-loop from the *XPB1* sequence.



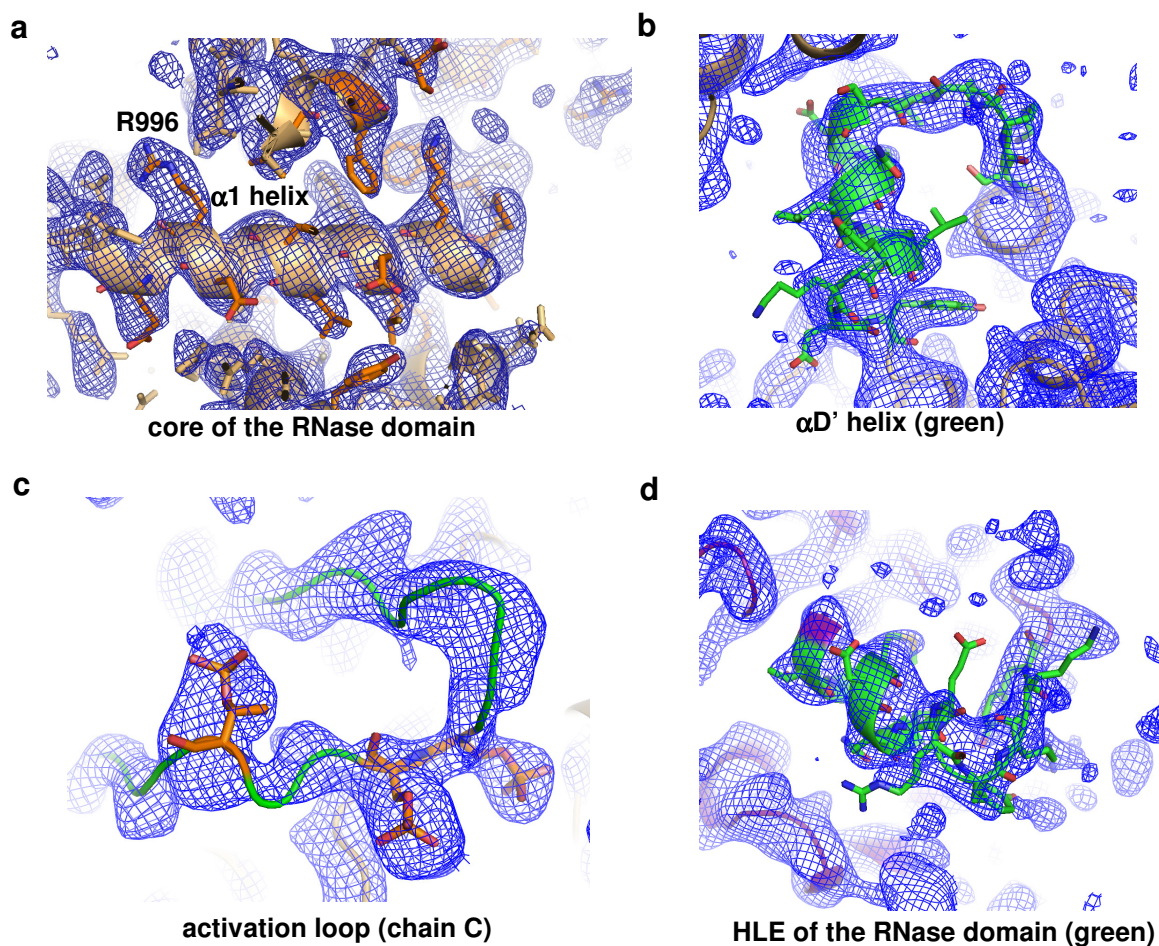
Supplementary Figure 2 | Activation profiles for cleavage of XBP1 443-mer by Ire1. Ire1KR32 undergoes a cooperative activation at low-nanomolar concentrations and exhibits a dramatically higher enzymatic activity during cleavage of XBP1 443-mer compared to reactions with HP21 RNA substrate (Fig. 1d). Ire1KR24 and Ire1KR do not exhibit a significant rate or cooperativity increase during cleavage of XBP1 443-mer compared to HP21. Reactions were conducted as in Fig. 1d and contained 0.05% Triton-X-100 to prevent Ire1 sticking to the walls of the reaction tube at low protein concentrations.



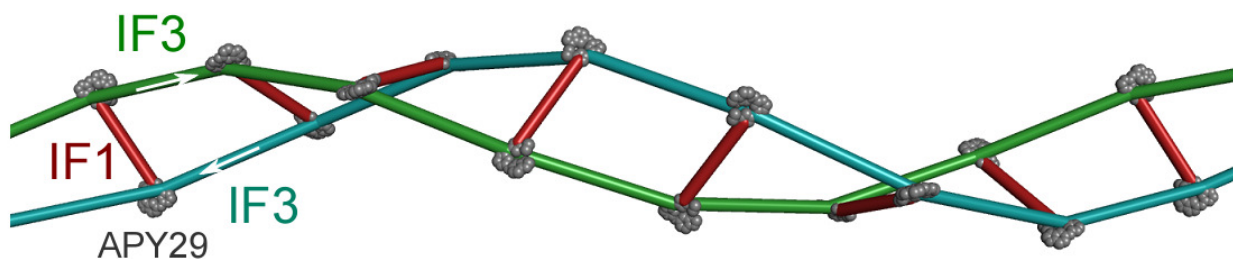
Supplementary Figure 3 | Activation of Ire1KR32 by ADP. Activation profile for cleavage of HP21 by Ire1KR32 (3 μM) in the presence of ADP. Conditions were as in Fig. 3a.



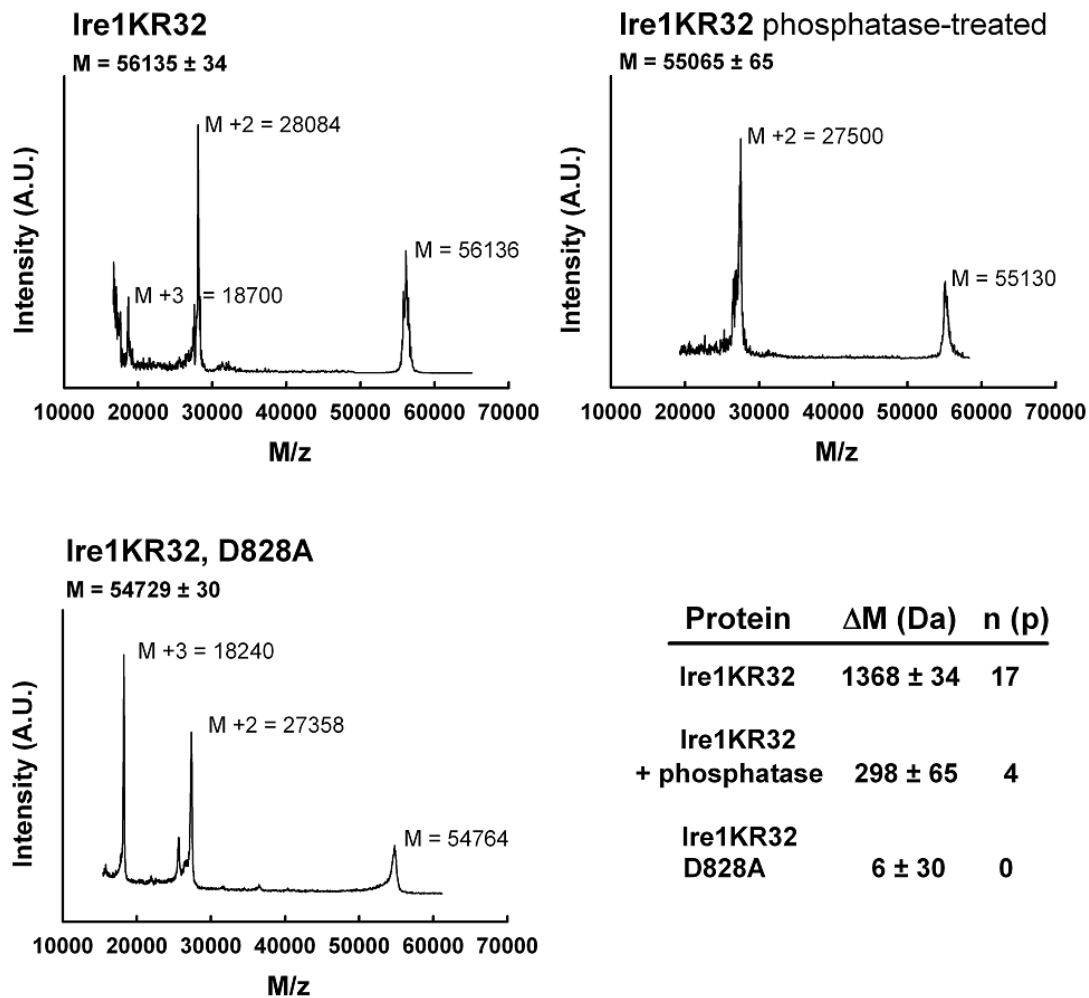
Supplementary Figure 4 | The effect of the disordered α F- α EF loop deletion on the RNase activity of Ire1KR32. Deletion of the α F- α EF loop that is disordered in the 3.9 Å crystal structure of the Ire1KR32 oligomer has no appreciable effect on the RNase activity. Ire1KR32 Δ 28 has the sequence of Ire1KR32 minus 28 amino acids of the α F- α EF loop (NNLQCQVETEHSSSRHTVVSSDSFYDPF). The poor reactivity of Ire1KR that lacks the N-terminus, the only other fragment that was disordered in the 3.9 Å crystal structure of the Ire1KR32 oligomer, is shown for comparison. Error bars show variability between single-exponential fits from two - five independent measurements.



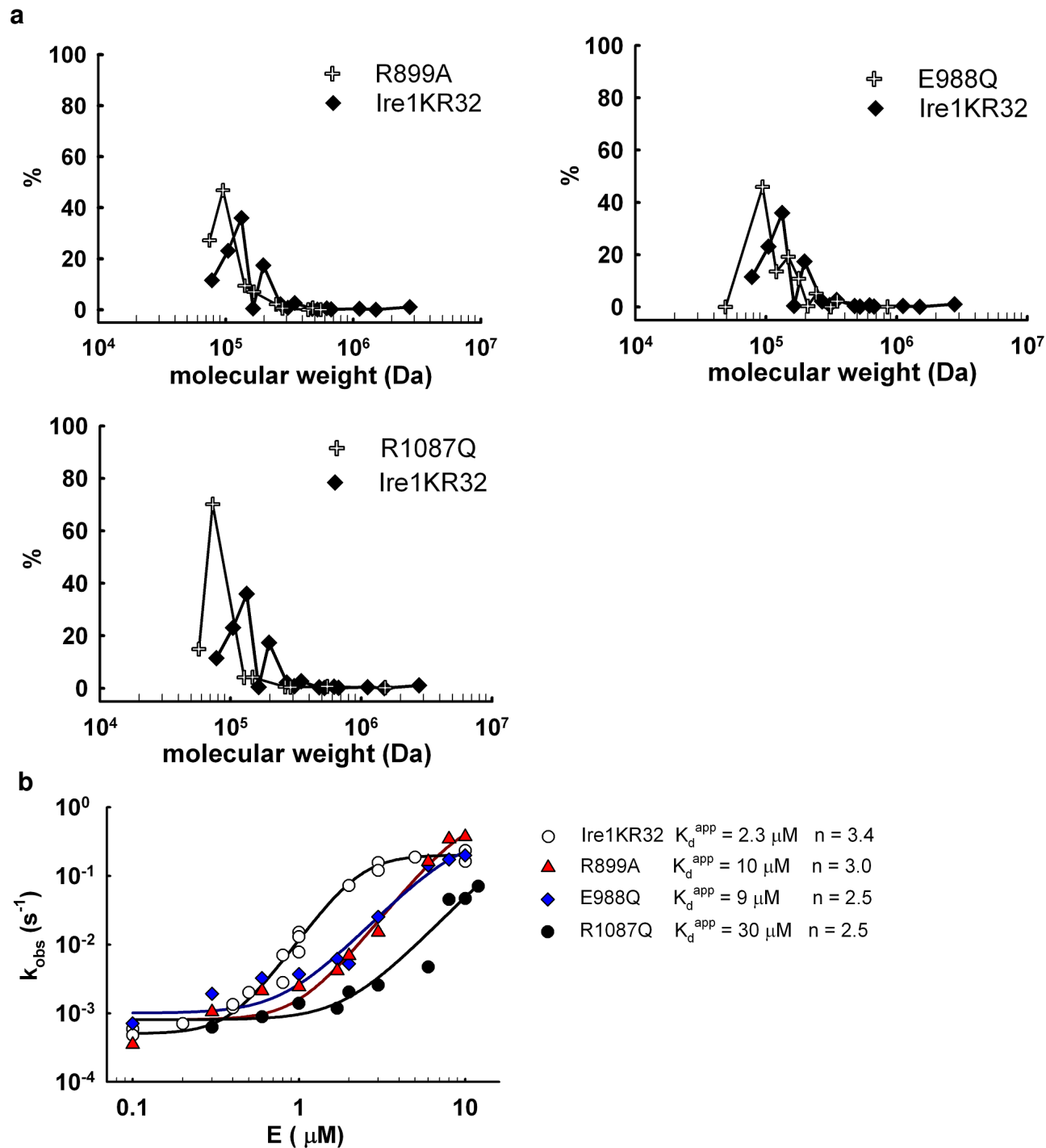
Supplementary Figure 5 | Representative examples of σ_A -weighted $3F_{\text{obs}}-2F_{\text{calc}}$ electron density maps for Ire1KR32 Δ 28 in the oligomer. **a, Electron density for the $\alpha 1$ helix of the RNase domain (contour level 1σ). **b**, Electron density for the $\alpha D'$ -helix of chain B (contour level 1σ). **c**, Electron density for the activation loop of chain C. Phosphates are shown in stick representation and are colored orange (contour level 1.5σ). **d**, Electron density for the $\alpha 3'$ helix and $\alpha 3'$ - $\alpha 4$ loop of the RNase domain (chain B) (contour level 1σ). Examples of simulated annealing omit maps are provided in Supplementary Fig. 13.**



Supplementary Figure 6 | Double-helical structure of the Ire1 oligomer. Double helix formed by connecting the active sites of the kinases in the Ire1 oligomer with straight lines. The red lines show the interface IF1. The green and the teal lines show the interface IF3 in two antiparallel strands. White arrows show the direction of phosphorylation loop donation. For reference, the molecules of APY29 at the active sites of the kinase domains are shown in gray.



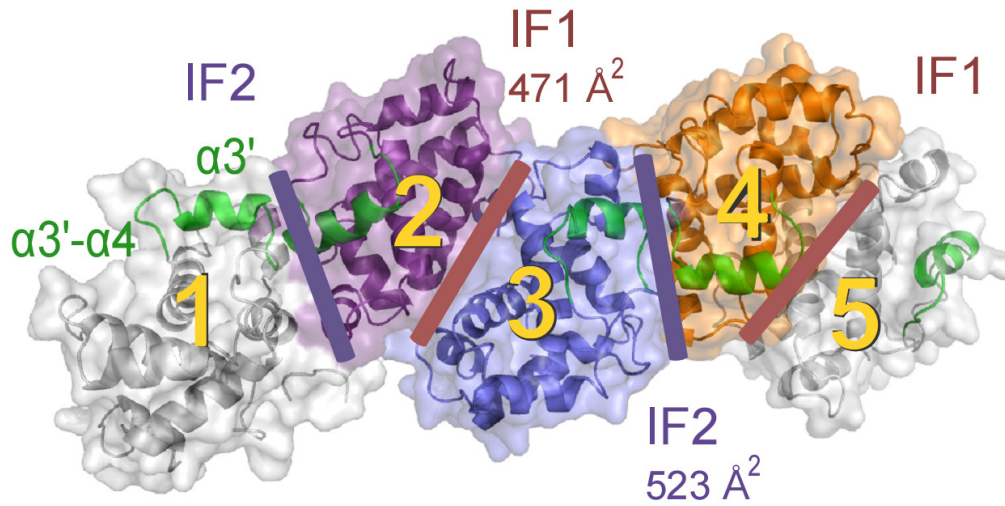
Supplementary Figure 7 | Mass spectra of Ire1KR32 reveal its phosphorylation status. MALDI spectra of Ire1KR32 before (top left) and after phosphatase treatment show the presence of 17 and 4 phosphates, respectively. Phosphatase treatment was done with a mixture of SAP and CIAP phosphatases for 1 hour at 30 °C. Mutation D828A that disrupts ATP•Mg coordination (Fig. 3e) results in a quantitative loss of Ire1 phosphorylation.



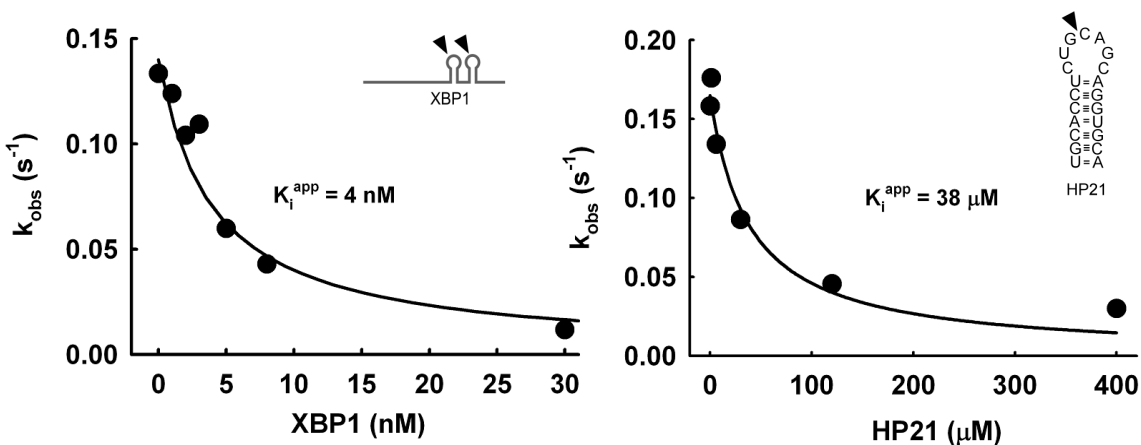
Supplementary Figure 8 | Characterization of the Ire1KR32 oligomer interface mutants. **a**, Analytical ultracentrifugation analysis of Ire1KR32 with disrupting point mutations at each of the three oligomerization interfaces. Mutations at each of the three

interfaces destabilize large assemblies indicating importance of all three crystallographically identified interfaces for Ire1KR32 oligomerization. Profiles of wild type IreKR32 are shown with diamonds, profiles of the mutants are shown with crosses.

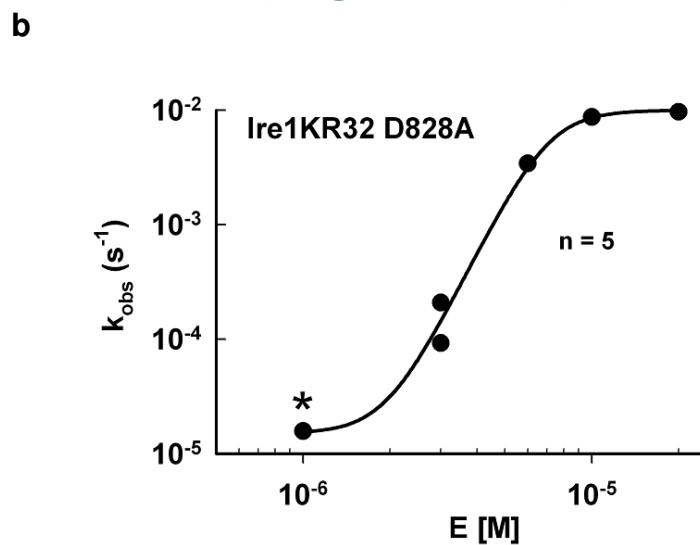
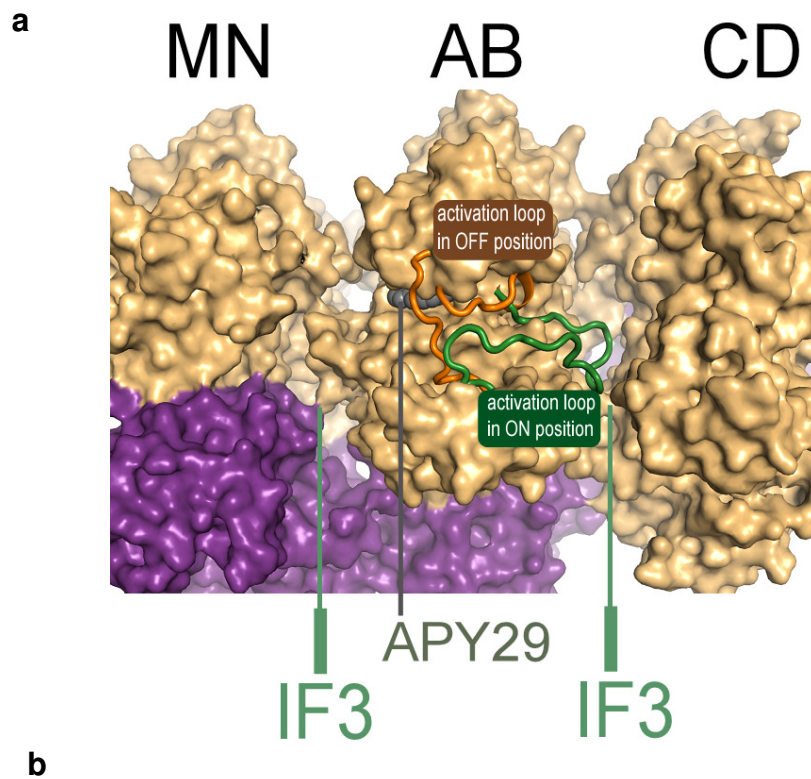
b, Activation profiles of Ire1KR32 with the interface mutations characterized in (a). Mutations at all three interfaces, IF1, IF2 and IF3, shift the activation profiles to the right revealing a weaker self-association capability of the mutants compared to wild type Ire1KR32.



Supplementary Figure 9 | Polymer structure of the RNase domain of Ire1KR32 and Ire1KR32Δ28. Five RNase monomers are shown and numbered. Total surface area buried upon formation of the IF1 and the IF2 are indicated. The helix-loop element (HLE) is shown in green.

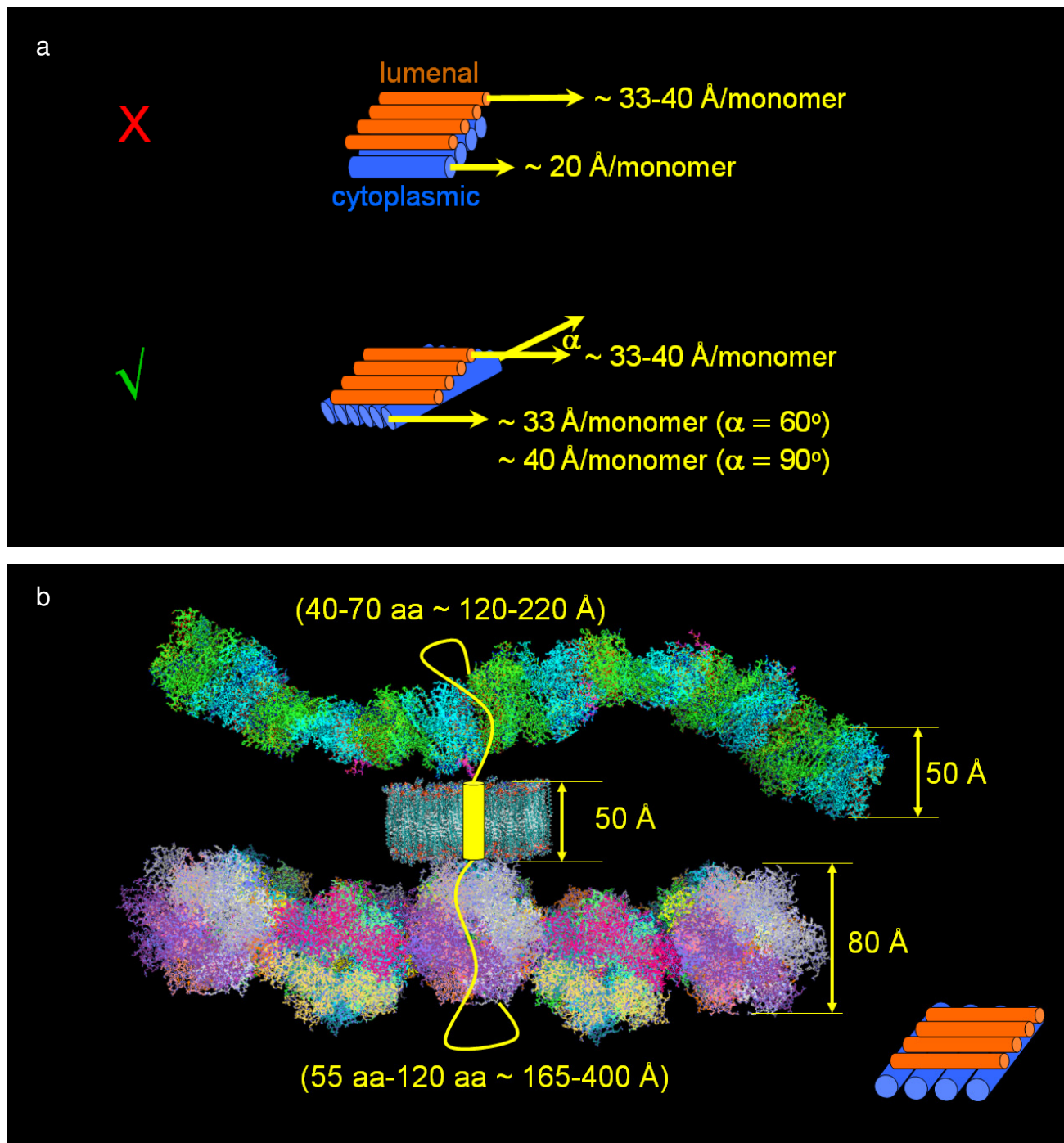


Supplementary Figure 10 | Binding of *XBP1* 443-mer and HP21 to Ire1KR32. a, Binding of *XBP1* mRNA to Ire1KR32 measured via inhibition of Ire1KR32-catalyzed cleavage of ^{32}P -*XBP1* by unlabeled *XBP1* mRNA. Reactions contained 5 nM Ire1KR32. Hyperbolic fitting of the data gave an apparent inhibition constant $K_i^{app} = 4 \text{ nM}$. **b,** Binding of HP21 to Ire1KR32 measured via inhibition of Ire1KR32-catalyzed cleavage of ^{32}P -HP21 by unlabeled HP21 oligoribonucleotide. Reactions contained 3 μM Ire1KR32. The apparent inhibition constant K_i^{app} is 38 μM .



Supplementary Figure 11 | The role of phosphorylation in the oligomer assembly of Ire1KR32. a, Position of the activation loop in the oligomer (green) corresponds to an open (phosphorylated) state of CDK2-type kinases. The activation loop points to

interface IF3 and forms intermolecular contacts with the acceptor kinase. For comparison, an activation loop in a closed state (orange) is shown as a model based on CDK2 kinase PDB ID 2C5Y. In the closed state, the activation loop of Ire1 would reside away from the interface IF3. **b**, The unphosphorylated variant of Ire1KR32 (D828A) activates cooperatively. Reactions were conducted as in Fig. 1d. Asterisk shows conditions marked (*) in Fig. 1d.

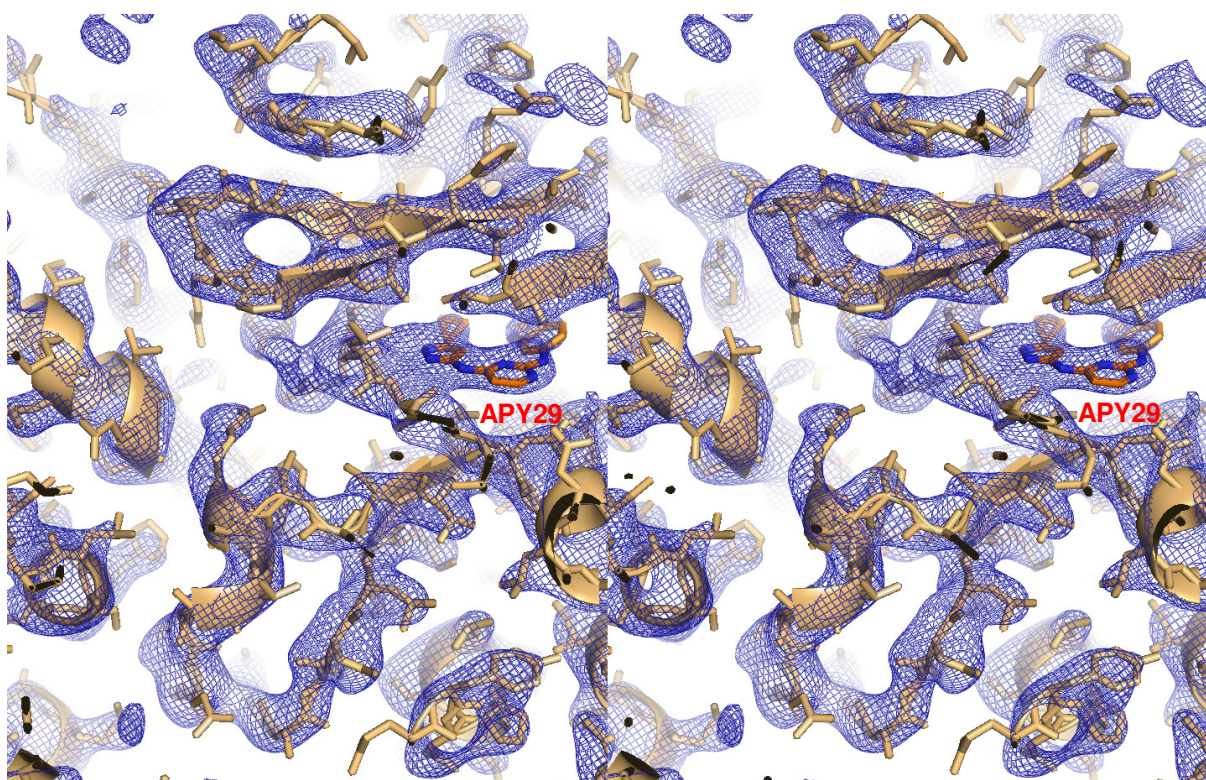


Supplementary Figure 12 | A model architecture of the Ire1 foci observed *in vivo*.

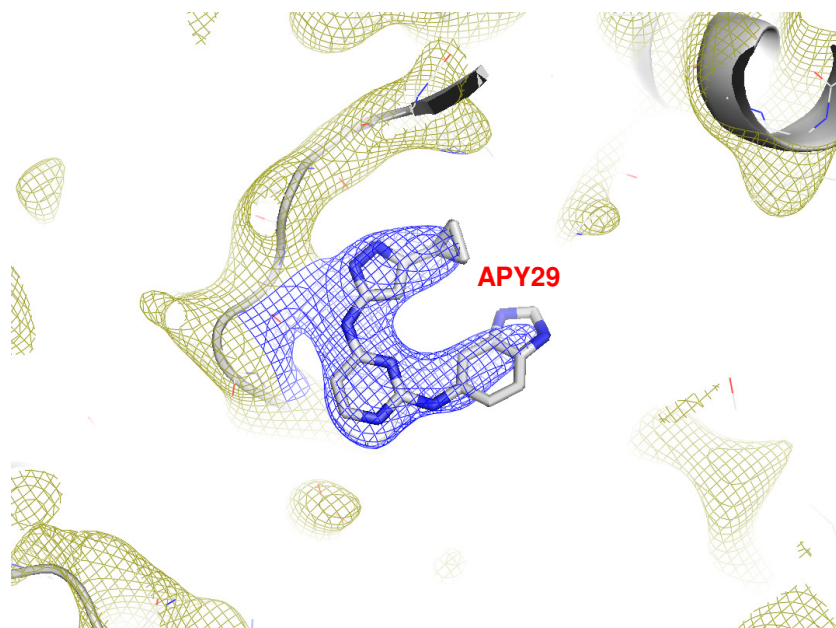
a, Comparison of the monomer packing density along the filament axis in the crystal

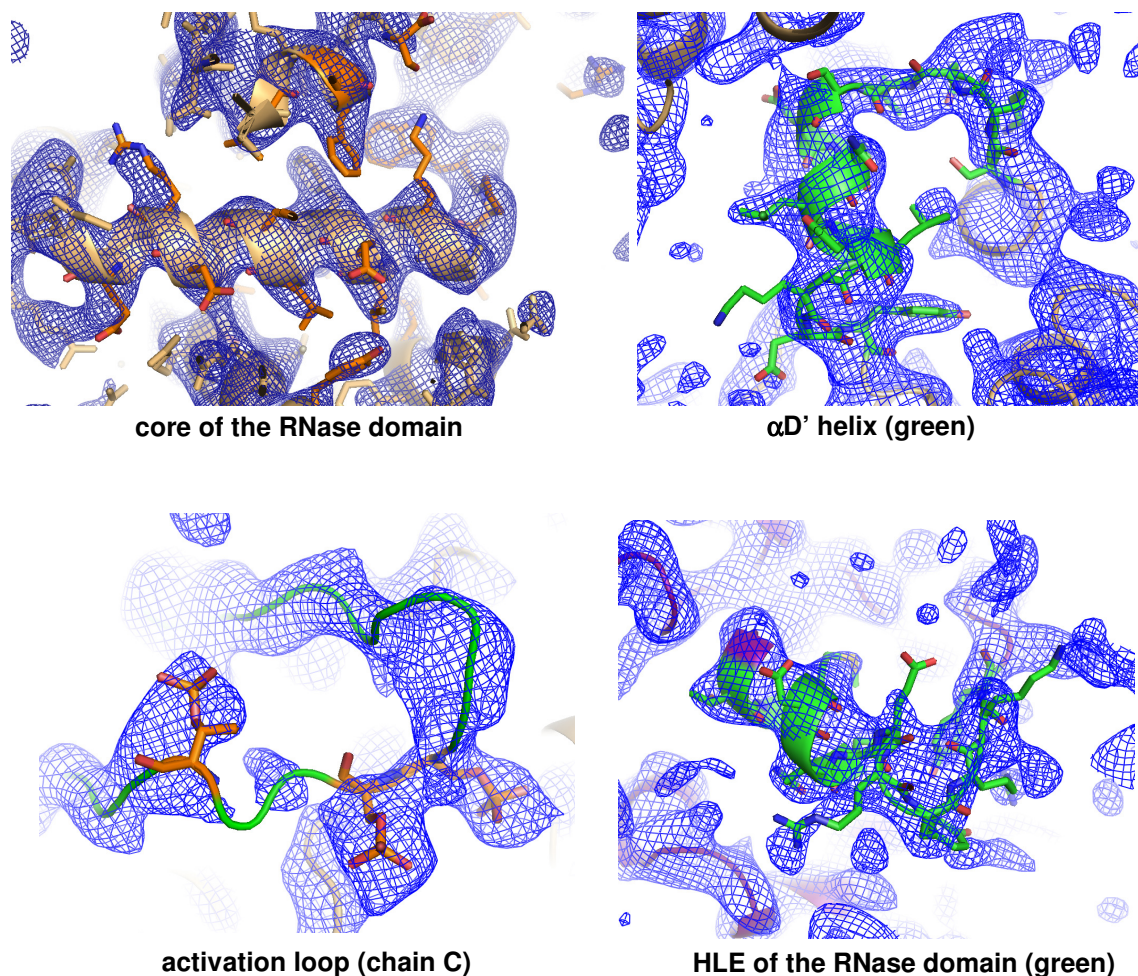
structures of the luminal domain (PDB ID 2be1, orange) and of the oligomeric cytoplasmic domain of Ire1 (PDB ID 3fbv, blue). Similar monomer density on the two sides of the ER membrane can be achieved with packing of the filament axes at a 60–90-degree angle. **b**, A filament of the oligomeric luminal domain (top), a modeled membrane (generated in VMD, UIUC) and several asymmetric units of the oligomeric cytoplasmic domain (oriented as in Fig. 4a, side view) are shown. The transmembrane (TM) region of Ire1 is shown as a yellow cylinder in the membrane. On each side of the membrane, linker lengths between the TM and the functional domains of Ire1 are sufficient to allow oligomerization even for monomers whose membrane-bound termini face away from the membrane. The variance in the number of amino acids and their respective calculated linear length for different organisms (human, mouse and yeasts) are shown.

a



b





Supplementary Figure 13 | Examples of simulated annealing omit maps. a, Simulated annealing composite omit map for a hydrophobic core of monomer A from the oligomer formed by Ire1KR32 Δ 28. Stereo view of the simulated-annealing σ_A -weighted 3Fo-2Fc composite omit map obtained without NCS restraints. Contour level is 1σ . **b,** Representative examples of simulated annealing σ_A -weighted 3Fo-2Fc composite omit maps obtained with NCS restraints for several parts of the Ire1KR32 Δ 28 oligomer structure. Contour level is 1σ for APY29, α D' helix and α 3'-helix and 1.5σ for other regions.

Supplementary Table 1

Tryptic peptides absent in MALDI spectra of Ire1KR32*.

	Wild type	Kinase-dead
N-terminus	PEKKKRKRGSRGGKKGRKSR	PEKKKRKRGSRGGKKGRKSR
N-lobe	IIHR	LQK, IIHR
Activation loop	LDSGQSSFRTNLNNPSGT	
α EF- α F	SGWRAPELLEESNNLQCQVE TEHSSSR	
C-lobe and RNase	LTR, VLR, SK, YR, ALR, EFLYS	LTR, VLR, SK, YR, ALR, EFLYS

*Extensive phosphorylation of the activation loop and α EF- α F loop reduces their volatility and results in the absence of these fragments in the mass spectra of wild-type Ire1KR32 that contains 17 phosphates (Supplementary Fig. 7). Both of these fragments are observed for unphosphorylated Ire1KR32.

Supplementary Table 2

Data collection and refinement statistics

	Ire1KR32A28•APY29
Data collection	
Space group	P21212
Cell dimensions	
<i>a</i> , <i>b</i> , <i>c</i> (Å)	156.8, 163.5, 292.8
α , β , γ (°)	90, 90, 90
Resolution (Å)	48-3.32 (3.31-3.2)*
<i>R</i> _{pim} ^{&}	0.053 (0.342)
<i>I</i> / σ <i>I</i>	16 (2.2)
Completeness (%)	100 (100)
Redundancy	23.2 (23.0)
Refinement	
Resolution (Å)	3.2
No. reflections	2846271 (274977)
<i>R</i> _{work} / <i>R</i> _{free}	0.235 / 0.283
No. atoms	
Protein	47668
Ligand/ion	(APY) 350
Water	0
B-factors**	
Protein	96
Ligand/ion	(APY) 81
R.m.s deviations	
Bond lengths (Å)	0.006
Bond angles (°)	0.910

A single crystal was used for data collection.

*Highest resolution shell is shown in parenthesis.

**Average B-factors were calculated from the model after grouped isotropic B-factor refinement in CNS¹. These differ from the TLS-derived components of anisotropic B-factors reported in the final structure.

[&]Precision-indicating merging R-factor²

Supplementary Table 3

Real-space R-factors for each of the monomers of the asymmetric unit calculated against corresponding simulated-annealing $2F_{\text{obs}} - F_{\text{calc}}$ omit maps.

Monomer	R-factor
A	0.161
B	0.168
C	0.163
D	0.164
E	0.166
F	0.169
G	0.175
H	0.179
I	0.190
J	0.189
K	0.182
L	0.179
M	0.170
N	0.165

Supplementary Table 4

Isotropic B-factors of the interface residues chosen for mutations (Fig. 5) obtained in CNS by B-group refinement.

Residue	B-factor
K992, monomer A (B)	69 (68)
E988, monomer B (A)	83 (81)
E1067, monomer A	149
R947, monomer D	98
D1030, monomer A (D)	113 (119)
R1087, monomer D (A)	73 (73)
Y1083, monomer A (D)	75 (77)
R899, monomer C	77
D763, monomer A	135

Supplementary Table 5

Distribution of R_{pim} versus resolution for the Ire1 Δ 28•APY29 co-crystal.

Resolution (Å)	R_{pim}
12.39	0.010
8.76	0.010
7.16	0.015
6.20	0.025
5.54	0.036
5.06	0.040
4.68	0.039
4.38	0.051
4.13	0.067
3.92	0.106
3.74	0.140
3.58	0.174
3.44	0.225
3.31	0.290
3.20	0.342

1. Brunger, A. T. et al. Crystallography & NMR system: A new software suite for macromolecular structure determination. *Acta Crystallogr D Biol Crystallogr* **54**, 905-21 (1998).
2. Weiss, M. S. Global indicators of X-ray data quality. *J. Appl. Cryst.* **34**, 130-135 (2001).